A process-oriented analysis of the summertime diurnal cycle of precipitation and diabatic heating over China in three reanalyses

Yanjie Liu[1, 2], Xiaocong Wang[3], Yimin Liu[1, 2], Shuaiqi Tang[4], Hao Miao[5, 6]

[1]State Key Laboratory of Earth System Numerical Modeling and Application, Institute of Atmospheric Physics, Chinese
5 Academy of Sciences, Beijing, 100029, China
[2]College of Earth and Planetary Sciences, University of Chinese Academy of Sciences, Beijing, 100049, China
[3]Institute of Atmospheric Physics, Chinese Academy of Sciences, Beijing, 100029, China
[4]School of Atmospheric Sciences, Nanjing University, Nanjing, 210023, China
[5]Nanjing Innovation Institute for Atmospheric Sciences, Chinese Academy of Meteorological Sciences–Jiangsu
10 Meteorological Service, Nanjing, 210041, China
[6]Jiangsu Key Laboratory of Severe Storm Disaster Risk / Key Laboratory of Transportation Meteorology of CMA, Nanjing,
210041, China

Submitted to Atmospheric Chemistry and Physics

Correspondence to: Xiaocong Wang (wangxc@lasg.iap.ac.cn)

Abstract. We conduct a process-oriented analysis of the summertime diurnal cycle of precipitation (DCP) over China by comparing three widely used reanalyses (ERA5, JRA-55, and MERRA-2) with satellite observations. While all reanalyses capture the observed nocturnal precipitation peak related to elevated convection, they differ substantially in simulating the
20 daytime rainfall timing. JRA-55 and MERRA-2 better capture the observed timing, whereas ERA5 exhibits a systematic 3-hour phase advance. The superior performance of JRA-55 is attributed to its gradual development of deep convection, supported by sustained heating and convective eddy transport. In contrast, ERA5 develops deep convection too rapidly, resulting in premature peaks in heating and precipitation. MERRA-2 also produces early-peaking convective rainfall, but with notably weaker intensity, suggesting that its better diurnal cycle is achieved largely through the suppression of convective
25 precipitation. Diurnal cloud structures further corroborate these differences. Whereas JRA-55 exhibits a slowly developing, upward-tilting cloud structure from morning to afternoon, ERA5 and MERRA-2 peak earlier and have a shorter duration. The role of large-scale forcing, quantified by CAPE and dynamic CAPE (dCAPE), is further tied to the performance of the convection schemes. Results show the peak timing of dCAPE lags that of CAPE and aligns more closely with the observed precipitation. While convective precipitation in ERA5 and MERRA-2 tracks CAPE more closely, in JRA-55 it aligns better
30 with dCAPE, thereby yielding a more realistic DCP. This contrast highlights the critical influence of triggering choice on cumulus convection.

1 Introduction

The diurnal cycle of precipitation (DCP) is a fundamental mode of precipitation cycles in the climate system. It influences local evapotranspiration and gross primary productivity, with direct implications for agricultural productivity and economic outcomes (Yang et al., 2023). Spatially, DCP is shaped by local to large-scale dynamic and thermodynamic processes (Dai, 2001; Trenberth et al., 2003; Bao and Zhang, 2013). Over land, the diurnal cycle is typically dominated by an afternoon-to-evening convective peak driven by solar heating, as observed over continental interiors and mid-latitude plains (Dai, 2001; Li et al., 2008; Pradhan et al., 2025). In contrast, on the leeside of mountainous regions, such as the Tibetan Plateau, the Rockies, and the Andes, nocturnal rainfall dominates due to terrain–circulation interactions (Carbone and Tuttle, 2008; Zhang et al., 2014). Accurate simulation of DCP is crucial to advancing the precision of the "timing–location–intensity" in fine-scale forecasting, particularly for extreme precipitation on sub-daily timescales (Trenberth et al., 2003; Dai and Trenberth, 2004; Chen et al., 2017). However, even state-of-the-art numerical models continue still show persistent systematic biases, notably a premature afternoon peak over land and a common failure to capture nocturnal rainfall maxima (Lee et al., 2007; Covey et al., 2016).

In seeking to explain these DCP simulation biases, previous studies attributed the deficiencies to shortcomings in convection parameterization schemes (e.g., Koo and Hong, 2010). A key factor contributing to these shortcomings lies in trigger mechanisms. Many schemes initiate convection based on convective available potential energy (CAPE), which responds rapidly to solar heating, resulting in overly frequent and premature triggering of afternoon convection (e.g., (Xie and Zhang, 2000; Lee et al., 2007; Yang et al., 2018). Additionally, the use of fixed entrainment rates and a rigid separation between shallow and deep convection can produce an abrupt and unrealistic regime transition (Bechtold et al., 2004; Khairoutdinov and Randall, 2006; Rio et al., 2009; Song et al., 2018). On the other hand, the widespread inability to capture nocturnal precipitation maxima is often linked to the failure of parameterizations in representing elevated convection originating from above the planetary boundary layer (Lee et al., 2008; Wang et al., 2015; Xie et al., 2019b). To overcome these limitations in convection parameterizations, several targeted refinements have been proposed. Xie and Zhang (2000) introduced dynamic CAPE (dCAPE) triggering, which initializes convection only when the large-scale forcing for CAPE production exceeds a critical value. The modification resulted in a better-represented thermodynamic structure and more accurate phase and amplitude in the simulated DCP (Xie and Zhang, 2000; Zhang, 2002; Xie et al., 2019b). Bechtold et al. (2008, 2014) incorporated moisture-dependent entrainment and accounted for CAPE consumption by boundary-layer turbulence and shallow convection, which helped reduce spurious morning precipitation peaks over land. To better represent nocturnal rainfall, Wang et al. (2015) designed a trigger function that allows air parcels to be lifted from above the boundary layer, enabling successful simulation of elevated nocturnal convection over the central Great Plains (Xie et al., 2019b; Wang et al., 2020).

Although the aforementioned modifications have mitigated certain biases in DCP simulation, current numerical models still struggle with a premature afternoon peak and the absence of a nocturnal rainfall signal (Tang et al., 2021, 2022; Tao et al., 2024). This limited success may be partially explained by the region-specific nature of these parameterization improvements. Many previous studies have primarily relied on sites from the Atmospheric Radiation Measurement (ARM) programme, especially the Southern Great Plains (SGP), to develop and evaluate their schemes (Xie and Zhang, 2000; Wang et al., 2015; Tang et al., 2022). Findings from these relatively homogeneous regions may not generalize well to areas with markedly different climatic and topographic contexts. This is particularly relevant for China, where complex terrain—including plateaus, basins, mountains, and plains—interacts with strong land–sea thermal contrasts and the East Asia monsoon, producing a highly diverse and regionally distinct DCP (Yu et al., 2007; Li et al., 2008). As a result, even state-of-the-art models often fail to accurately capture the timing and amplitude of the DCP over China (Yuan, 2013; Lin et al., 2019; Song and Wei, 2021). While previous studies have often linked these biases to large-scale meteorological conditions or topographic influences, there remains a lack of systematic efforts to link these errors to specific parameterized physical processes, underscoring the necessity of process-oriented analysis.

Reanalyses incorporate the most advanced operational parameterization suites; thus, a detailed assessment of their performance can offer critical insights into how key physical processes are represented and help guide future model development. Moreover, given their widespread use as benchmarks in model evaluation (Yuan, 2013; Ma et al., 2021; Zhang et al., 2024)(Yuan, 2013; Ma et al., 2021; Zhang et al., 2024), it is essential to rigorously assess how well they can serve as realistic references for diurnal precipitation studies (Wright et al., 2020). To this end, this study conducts a process-oriented evaluation of the diurnal cycle of precipitation and the associated diabatic heating over China using three widely-used reanalyses—ERA5, JRA-55, and MERRA-2. We move beyond simple pattern comparison and instead aim to unravel the physical mechanisms that underlie the differences among the reanalyses. Our analysis is framed by two guiding questions: 1) How do the reanalyses perform in representing the DCP over China, and where do they most notably differ? 2) What physical processes are responsible for these divergent behaviors? By linking discrepancies in precipitation timing to co-evolving physical processes, this study seeks to identify targeted pathways for improving the simulation of DCP across China. The remainder of the paper is structured as follows: Section 2 describes the data sources. Section 3 compares the characteristics of the DCP in reanalyses against satellite observations. Section 4 presents a detailed process-oriented diagnosis of heating, clouds, and eddy-transport fields. Section 5 discusses the role of large-scale forcing on DCP simulation. Finally, conclusions are summarized in Section 6.

2 Observation and Reanalysis Data

This study employs two complementary satellite-based precipitation products as observational references: the Integrated Multi-satellitE Retrievals for Global Precipitation Measurement (IMERG) Final Run Version 07B (Huffman et al., 2023) and the Climate Prediction Center Morphing Technique (CMORPH) Climate Data Record (Xie et al., 2019a). The IMERG dataset,

available from 2000 onward, provides global surface precipitation estimates at a 0.1° spatial resolution and a half-hourly temporal resolution. It uses the GPM Core Observatory as a calibration reference to unify precipitation measurements from an international satellite constellation through advanced inter-calibration and merging algorithms. The CMORPH product supplies bias-corrected and reprocessed global precipitation analyses at an 8 km spatial resolution and a 30-minute temporal
100   cadence, covering the period from January 1998 to the present. Both datasets show good agreement with ground-based observations and have been widely used in studying the DCP (Shen et al., 2010; Tang et al., 2021).

To evaluate the performance of reanalyses in representing DCP, three widely used reanalyses are selected: the fifth-generation European Centre for Medium-range Weather Forecasts (ECMWF) reanalysis (ERA5; Hersbach et al., 2020), the Japanese 55-
105   year Reanalysis (JRA-55; Kobayashi et al., 2015), and the Modern-Era Retrospective Analysis for Research and Applications, Version 2 (MERRA-2; Gelaro et al., 2017). ERA5 has a horizontal resolution of 0.25° and provides hourly output for surface and pressure-level variables. JRA-55 has a coarser grid of 1.25°, providing surface fields every 3 hours and pressure-level fields every 6 hours. MERRA-2 features an intermediate resolution of 0.5° × 0.625°, with surface variables available hourly and pressure-level variables every 3 hours. The analysis focuses on the boreal summer (June–July–August) during 2019–2023,
110   a period marked by strong diurnal precipitation signals over China.

3 Diurnal Cycle of Precipitation

3.1 Spatial Distribution of Diurnal Precipitation Phase and Amplitude

The diurnal phase and amplitude of precipitation were calculated using Fourier analysis, with the methodological procedure described in Appendix A. Figure 1 shows the diurnal peak time (local solar time, LST) of precipitation over China from the
115   observations and reanalyses. The two satellite products (IMERG and CMORPH) show high consistency. The spatial pattern displays pronounced regional heterogeneity, with a diurnal cycle dominated mainly by late-afternoon peaks and, secondarily, by nocturnal-to-early-morning peaks. Specially, the Tibetan Plateau, southeastern China, and northeastern China typically peak in the late afternoon or evening due to surface-driven convection. In contrast, adjacent lowlands such the Sichuan Basin and the Tarim Basin peak predominantly at night or in the early morning, influenced by mesoscale circulations like mountain–
120   valley breezes. Such wind systems often propagate convection downwind, yielding transition belts with phase delaying from afternoon to the following early morning, such as in the upper Yangtze River valley and the northern China (Bao and Zhang, 2013; Zhang et al., 2014).

In comparison, the three reanalyses exhibit distinct behaviours with notable regional discrepancies. JRA-55 reproduces the
125   observed phase pattern relatively well, capturing both afternoon and nocturnal peaks, although some late-afternoon peaks occur slightly earlier—for example, over northeast and southeast China. ERA5 broadly reproduces the regional contrasts, yet it exhibits a systematic phase-lead bias, with precipitation typically peaking 2–4 h earlier, particularly over the Tibetan Plateau,

southern China, and northeast China. MERRA-2 presents the most complicated spatial structure, mixing both leading and lagging phases within areas that appear phase-uniform in observations, such as the central Tibetan Plateau and western

130 southeastern China. Based on the phase characteristics described above, three representative regions with uniform peak times are selected (marked by boxes in Figure 1): the central Tibetan Plateau (TP, 30°–36°N, 88°–94°E), southeast China (SECN, 22°–28°N, 110°–120°E), and the Sichuan Basin (SCB, 28°–32°N, 103°–107°E). These areas encompass both nocturnal and late-afternoon rainfall regimes, making them suitable for analysis of the physical processes represented in reanalyses.
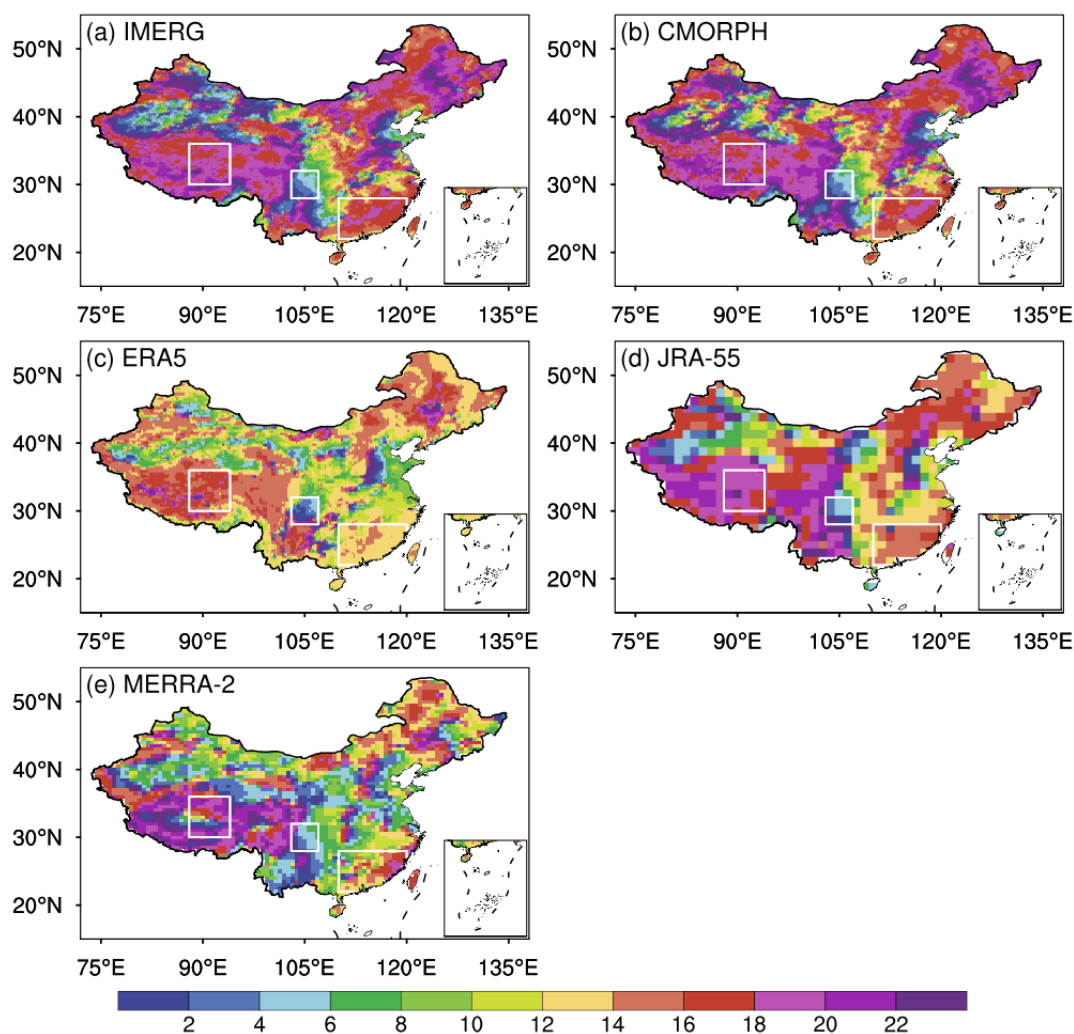
135 **Figure 1. Diurnal phase (local solar time, LST; the same hereafter) of total precipitation averaged over June–July–August (JJA) 2019–2023 for China from (a) IMERG, (b) CMORPH, (c) ERA5, (d) JRA-55, and (e) MERRA-2. White boxes mark the three representative regions: the Tibetan Plateau (TP, 30°–36°N, 88°–94°E), southeastern China (SECN, 22°–28°N, 110°–120°E), and the Sichuan Basin (SCB, 28°–32°N, 103°–107°E).**

140   The diurnal amplitude of precipitation is presented in Figure 2. IMERG and CMORPH show consistent spatial patterns across most of China, with pronounced amplitudes (>5 mm d^{-1}) predominating along the southeast coast, the Tibetan Plateau, and its downstream areas, whereas much weaker values (<1 mm d^{-1}) prevail over the northwest. Overall, all three reanalysis datasets capture this amplitude distribution reasonably well, although underestimation occurs in several regions. For instance, JRA-55 and MERRA-2 underestimate the DCP amplitude over SECN, whereas ERA5 underestimates it over SCB. These

145   underestimations stem largely from the inclusion of days whose diurnal phases deviate from the typical DCP of the target region.
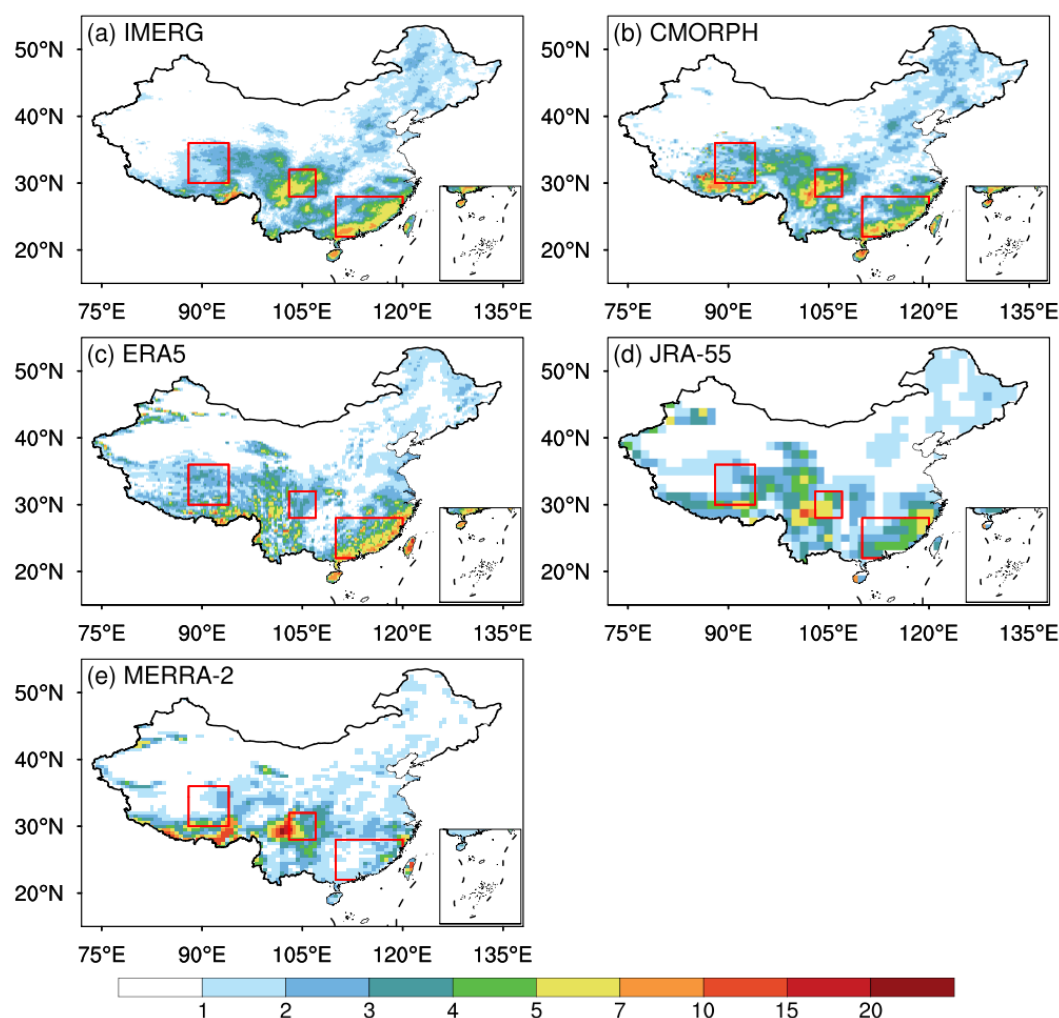
Figure 2. Same as Figure 1, but for diurnal amplitude (mm d^{-1}).

3.2 Composite Analysis

To isolate the typical DCP behaviour in the target regions, we performed a composite analysis by selecting precipitation events that represent the characteristic DCP category for each region. This composite approach excludes the influence of dry days, light precipitation, and days with diurnal phases inconsistent with the target regime. The year 2021 was chosen for this analysis; results from other years are similar. According to the China Meteorological Administration (CMA) standard, light rainfall is defined as a daily rate below 10 mm d^{-1}. For the relatively dry Tibetan Plateau (TP), this threshold was lowered to 5 mm d^{-1} following Zhang et al. (2021). Following the approach of Tang et al. (2021), afternoon-rainfall days were selected for TP and SECN (with precipitation peaks between 12:00 and 20:00 LST), and nocturnal-rainfall days were defined for SCB (peaks between 20:00 and 08:00 LST) to isolate the dominant diurnal signal. In all cases, the daily maximum precipitation must exceed the corresponding light-rain threshold. The selection criteria and number of selected events for the three key regions are provided in Table 1.

Table 1. Selection Criteria and Number of Selected Events in the Three Representative Regions

Criteria		TP	SECN	SCB
Peak time range (LST)		12:00 – 20:00	12:00 – 20:00	20:00 – 08:00
Threshold (mm d^{-1})		5	10	10
	GPM	49	42	52
	CMORPH	60	36	55
Number of selected events	ERA5	72	58	52
	JRA-55	73	32	59
	MERRA-2	20	19	59

Figure 3 compares the five-year JJA-averaged and case-composite diurnal variation of precipitation over the three regions. The composite cycles align closely with the multi-year mean in terms of phase, and the diurnal signals are amplified due to the removal of light-precipitation days, confirming that the selected cases dominate the diurnal signal and are representative for subsequent process analysis. Over TP and SECN, both IMERG and CMORPH exhibit a late afternoon peak near 18:00 LST, whereas SCB exhibits a distinct nocturnal maximum around 03:00 LST. Compared to observations, JRA-55 and

MERRA-2 reproduce these diurnal variations reasonably well over TP but, a slight phase advance of 1~2 hours over SECN. Over both TP and SECN, ERA5 initiates rainfall too early, producing a peak around 15:00 LST—about 3 hours ahead of the observed peak. All three reanalyses reproduce the nocturnal rainfall peak over SCB, yet ERA5 shows considerable underestimation in magnitude.
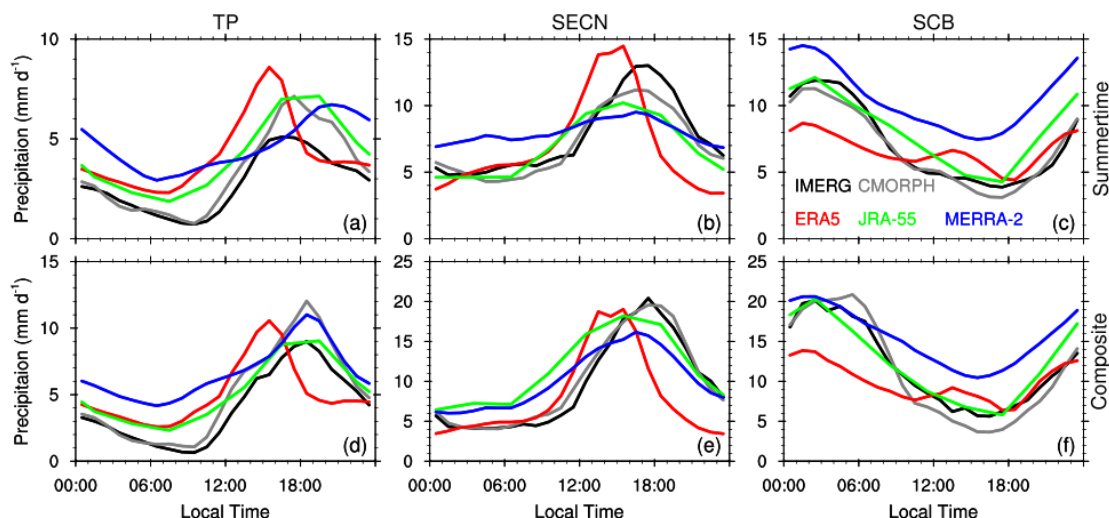
Figure 3. Five-year JJA-averaged (top row) and case-composite (bottom row) diurnal variations of precipitation over TP (left), SECN (middle) and SCB (right).

To distinguish the contributions of different rainfall process in models, Figure 4 shows the separate diurnal cycles of convective and large-scale precipitation. Over TP and SECN, the diurnal variations in both ERA5 and JRA-55 are dominated by convective precipitation, while the large-scale precipitation remains low (<3 mm d^{-1}). This suggests that the DCP behaviours of JRA-55 and ERA5 stem largely from their convection parameterization schemes. Over SCB, convective and large-scale precipitation in these two reanalyses contribute roughly equally to the total precipitation. In contrast, across all three regions, the diurnal variation in MERRA-2 is driven mainly by large-scale precipitation. Its convective rainfall is notably weaker and peaks earlier, like ERA5, indicating that MERRA-2 achieves the "right" diurnal cycle primarily through the suppression of convective precipitation.
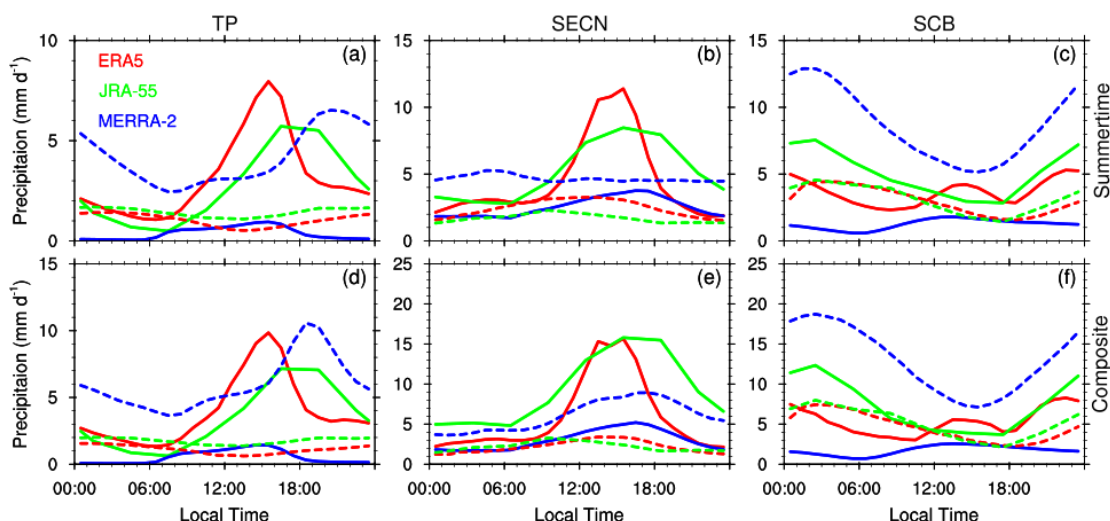
Figure 4 Same as Figure 3, but for convective (solid lines) and large-scale (dashed lines) precipitation.

The diurnal variation of cumulus mass flux, shown in Figure 5, provides further support for the physical interpretations described above. Because this variable is not archived in ERA5, only results from JRA-55 and MERRA-2 are shown. In JRA-55, the cumulus mass flux over TP peaks in the afternoon at approximately 30 kg m^{-2} s^{-1} and extends through a depth of 350 hPa. Over SECN, the flux originates from a lower altitude and deepens more markedly, consistent with heavier rainfall there relative to the TP. Over SCB, the flux peaks nocturnally at a much lower magnitude, around 8 kg m^{-2} s^{-1}. These flux behaviours align generally with the timing and intensity of convective rainfall in the corresponding regions. Compared to JRA-55, the cumulus mass flux in MERRA-2 is significantly weaker and shallower, with magnitudes mostly remaining below 12 kg m^{-2} s^{-1}. This limited convective intensity is consistent with the model's previously noted dependence on large-scale precipitation to shape the diurnal cycle.
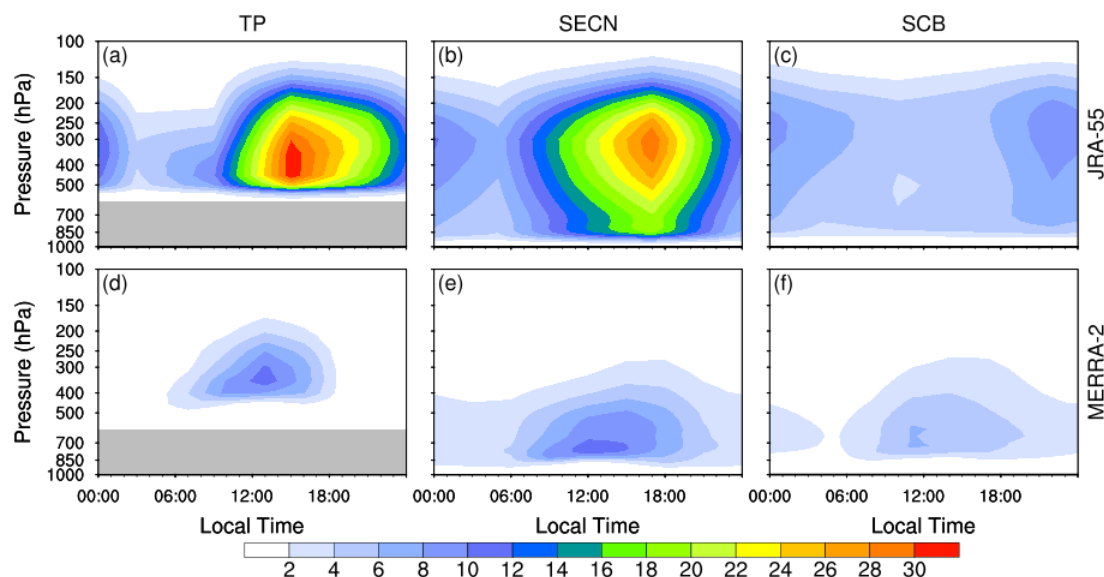
Figure 5. Diurnal variation of cumulative mass flux (kg m⁻² s⁻¹) for selected cases from JRA-55 (top row) and MERRA-2 (bottom row) over TP (left), SECN (middle) and SCB (right).

4 Diurnal Cycle of Heating and Clouds

To identify the physical processes responsible for the differences in simulated diurnal precipitation, we conduct a process-oriented analysis by comparing diabatic heating and cloud structures between different reanalyses.

4.1 Diabatic Heating

Figure 6 presents the diurnal cycle of apparent head source Q_1 and moisture sink Q_2 over the TP, with the diurnal-mean components removed. In all three reanalyses, the diurnal anomalies of Q_1 over TP exhibit a tilting structure extending from the surface to the mid-troposphere, with a maximum that initially lies in the boundary layer and ascends during the day. In the morning, heating remains concentrated in the lower layers driven by boundary layer turbulence and shallow convection. This stage is marked by a distinct negative peak in Q_2, indicating that moistening from turbulent and convective-scale transport exceeds condensation. As deep convection develops later, both Q_1 and Q_2 turn positive above the boundary layer. Comparatively, ERA5 shows a particularly rapid and deep development of Q_1, which peaks around 15:00 with a heating anomaly of 0.2 K h⁻¹ extending to 200 hPa. Concurrently, Q_2 reaches its maximum, though its magnitude remains substantially lower than that of Q_1—a difference linked to contrasting subgrid-scale transport of heat and moisture. JRA-55, by contrast, exhibits a weaker and more gradual evolution, with mid-level heating anomalies persisting until 21:00 LST, consistent with

its prolonged precipitation into the evening. MERRA-2 produces strong low-level heating and moistening in the morning, followed by an early upper-tropospheric heating peak around 13:00 LST. After 15:00 LST, precipitation-induced evaporation causes pronounced low-level cooling—a signature typical of stratiform clouds—suggesting an increasing contribution from

220 stratiform precipitation in the afternoon. These contrasts are further manifested in the vertical eddy transport of moist static energy ($Q_1-Q_2-Q_{rad}$). In JRA-55, subgrid-scale transport is initially confined to the boundary layer in the morning by turbulence, and later extends upward to 200 hPa by 15:00 LST and lasts into the evening by convection, in line with its sustained cumulus mass flux (Figure 5a). In ERA5, convective eddy transport rapidly reaches the upper troposphere by 12:00 LST and forms a center between 200–250 hPa around 15:00 LST, resulting in an earlier precipitation peak. In MERRA-2,

225 subgrid-scale eddy transport is mostly limited to below 400 hPa and peaks as early as 13:00 LST, a shallow, early structure indicative of suppressed convection (Figure 5d). These results demonstrate that the relatively gradual deepening of convection in JRA-55 yields precipitation timing closer to observations, whereas the overly rapid convective development in ERA5 yields earlier, stronger peaks. In MERRA-2, active boundary-layer turbulence and shallow convection promote premature convective rainfall and largely inhibit the full development of deep convection.
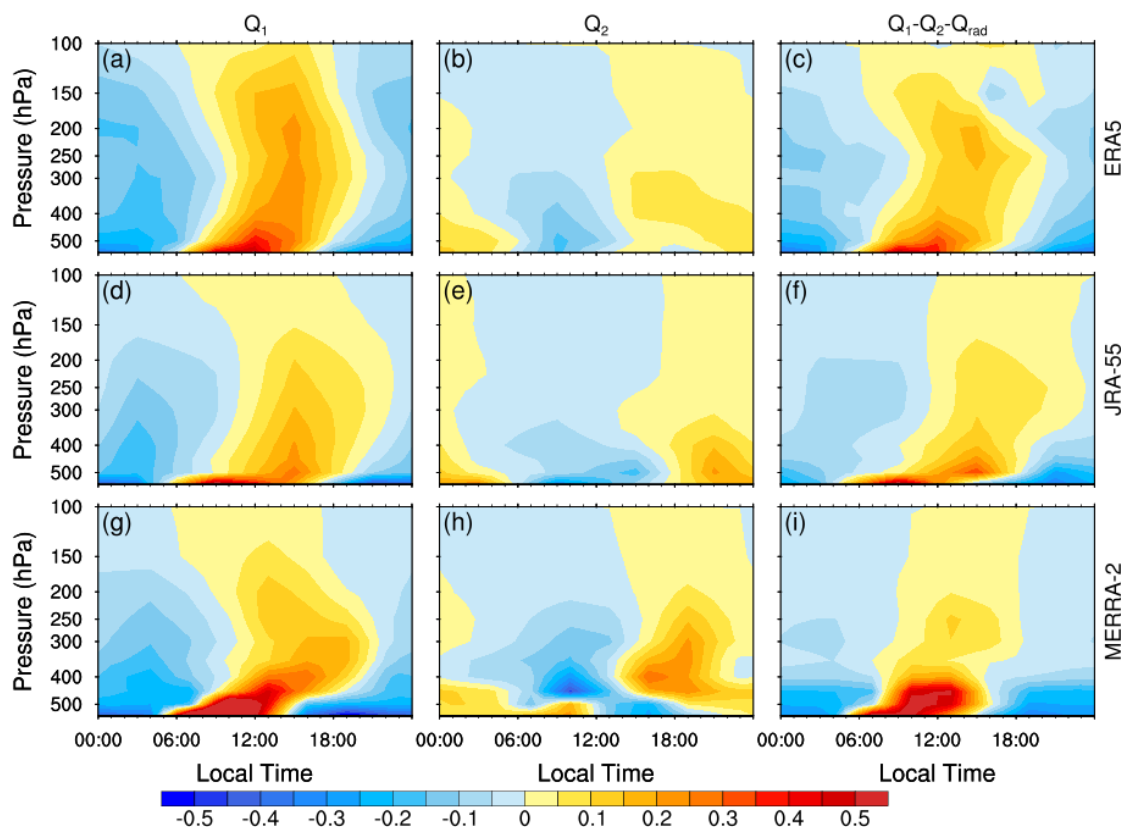
Figure 6. Diurnal variations of Q_1, Q_2 and $Q_1-Q_2-Q_{rad}$ anomalies over TP from ERA5 (top), JRA-55 (middle) and MERRA-2 (bottom). Units: K h^{-1}.

The discrepancies among the three reanalyses are more pronounced over SECN (Figure 7). Although the diurnal evolution of
235   heating and drying is similar to that over TP, convective systems penetrate more deeply in SECN. The heavier precipitation
generated by these deep systems increases the role of condensational heating relative to subgrid-scale eddy transport. As a
result, the vertical profiles of Q_1 and Q_2 become more alike above 700 hPa and their diurnal phases align closely. Only JRA-
55 maintains an obviously tilted heating structure, with deep convection developing gradually, peaking near 17:00 LST, and
persisting until about 21:00 LST. As over TP, ERA5 exhibits overly rapid development of deep convection over SECN, leading
240   to premature peaks in heating and subgrid-scale transport above 500 hPa and thus an earlier precipitation phase around 14:00
LST. Although the moister SECN environment is conducive to deep convection, MERRA-2 continues to exhibit overly strong
low-level heating and moistening while suppressing deep convection. Its subgrid-scale transport (>0.05 K h^{-1}) remains mostly
below 500 hPa, markedly shallower than in ERA5 or JRA-55, consistent with the model's weaker convective rainfall
contribution.

245
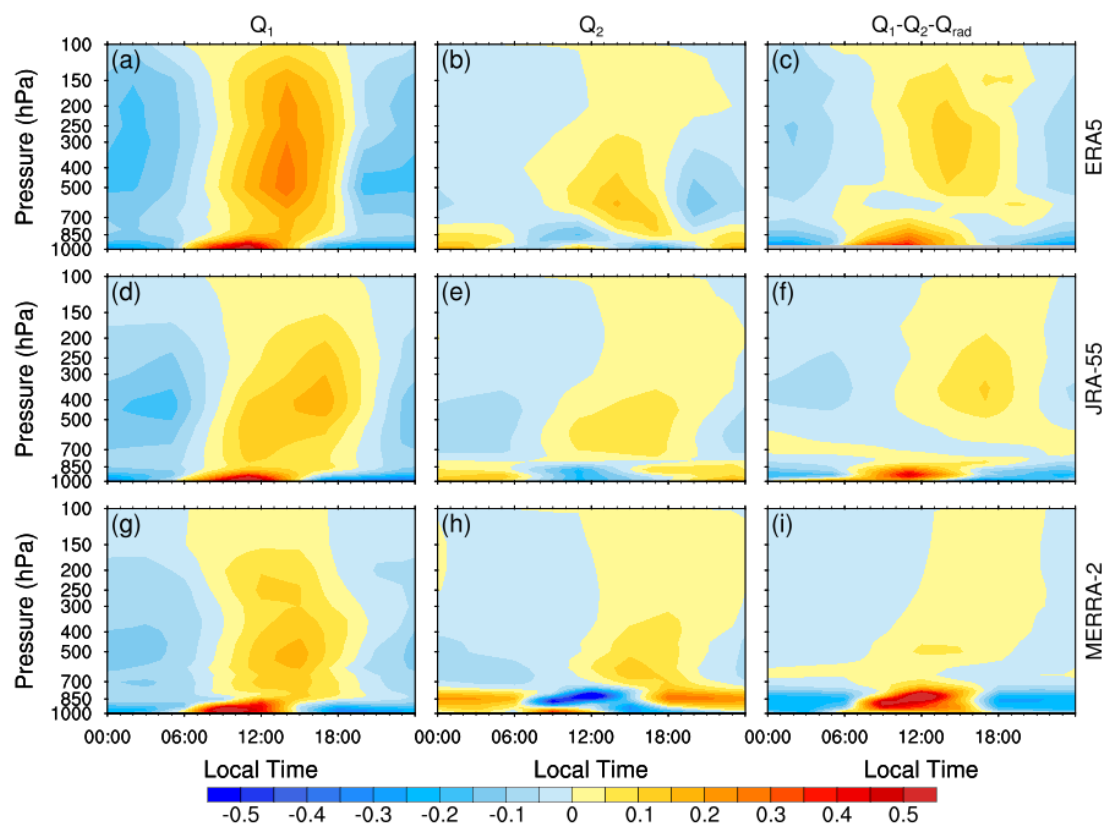
Figure 7. Same as Figure 6, but for SECN.

The evolution of diabatic heating over SCB differs markedly from that over TP and SECN (Figure 8). All three reanalyses
exhibit a consistent nocturnal pattern, with heating in the mid-troposphere and cooling in both the lower and upper levels. The

250 low-level negative Q_1 anomaly originates mainly from evaporative and radiative cooling, while the upper-level anomaly is a
consequence of the larger daytime upward heat flux. Meanwhile, Q_2 exhibits a column-wide negative anomaly during the day,
driven by moisture transport associated with turbulence and convection, and turns positive at night when condensation
dominates. Consequently, the vertical eddy-transport structure over the SCB is distinct. While boundary-layer turbulent and
convective eddy transport coincide during the day over the TP and SECN, they are temporally separated over SCB, with
255 convective eddy transport from elevated convection peaking at night. Among the three reanalyses, JRA-55 exhibits the most
coherent nocturnal evolution, with peaks in heating and convective eddy transport around 04:00 LST that align with its
strongest nocturnal convective precipitation. In comparison, ERA5 produces earlier nocturnal peaks, particularly in eddy
transport above 500 hPa, which maximizes after sunset and is accompanied by positive anomalies near 300 hPa during the
daytime. This structure indicates that ERA5 also triggers weak free convection after noon, consistent with its dual-peak
260 structure in convective precipitation. Although MERRA-2 generates the strongest nocturnal heating, its associated convective
eddy transport is the weakest, in line with its suppressed convection.
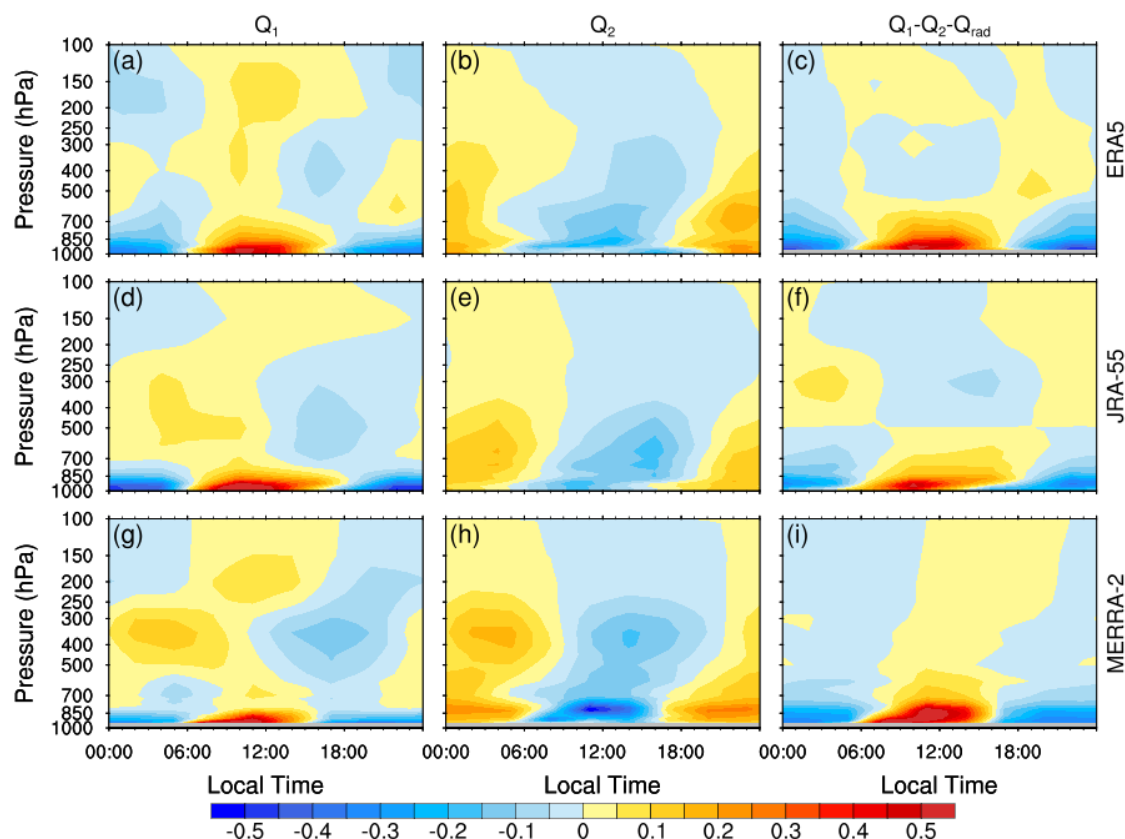
Figure 8. Same as Figure 6, but for SCB.

4.2 Cloud Vertical Structure

The aforementioned differences in physical processes are also reflected in cloud structures. Figures 9 and 10 present the vertical distribution of cloud fraction and cloud hydrometeor content. Over TP and SECN, both ERA5 and JRA-55 exhibit a slowly developing, upward-tilting cloud structure from morning to afternoon, with low-level clouds deepening progressively through a layer of about 200 hPa above the boundary layer. The deepening occurs in tandem with increasing cloud hydrometeor content, suggesting well-coordinated cloud macro- and microphysical representations in both reanalyses. In ERA5, the development of low-level cloud fraction and cloud water peaks earlier and is shorter in duration, consistent with its faster eddy transport and earlier precipitation maximum. In MERRA-2, however, cloud water shows a tilting vertical structure that is not mirrored in cloud fraction. Moreover, its cloud water content extends beyond 250 hPa, substantially deeper than in the other two datasets. In the upper troposphere, high-level clouds in both ERA5 and JRA-55 peak after deep convection decays. During the shallow-to-deep convective transition, ERA5 produces a notably larger cloud ice content, accompanied by a continuous band of high ice values ascending from lower levels in the afternoon. JRA-55 also shows increased cloud ice, but its ice content remains much lower than in ERA5, likely due to overly strict liquid-to-ice conversion criteria in its host model (Wright et al., 2020). MERRA-2 exhibits weaker diurnal variation in high-level clouds, yet its cloud ice content varies markedly. Given the excessively weak deep convection noted earlier, such substantial ice amounts cannot be explained solely by convective transport. Instead, they probably result from an overestimation of high-topped clouds in the model (Miao et al., 2019), a compensation designed to reduce the overly high outgoing longwave radiation that would otherwise arise from overly shallow convection and low detrainment heights (Molod et al., 2015). This compensating mechanism favours stratiform over convective precipitation, further supporting the view that stratiform processes dominate in MERRA-2. Over SCB, all three reanalyses exhibit a bimodal cloud fraction structure, with peaks near 175 hPa and 600 hPa. Again, ERA5 maintains good consistency between cloud hydrometeor and cloud fraction. Compared to ERA5, JRA-55 remarkably underestimates high-topped clouds, whereas MERRA-2 underestimates low-topped clouds, in consistency with the findings of Miao et al. (2019). These results underscore that while all three reanalyses reproduce basic cloud features, their physical coherence varies considerably, which in turn impacts the fidelity of the simulated diurnal cycle.
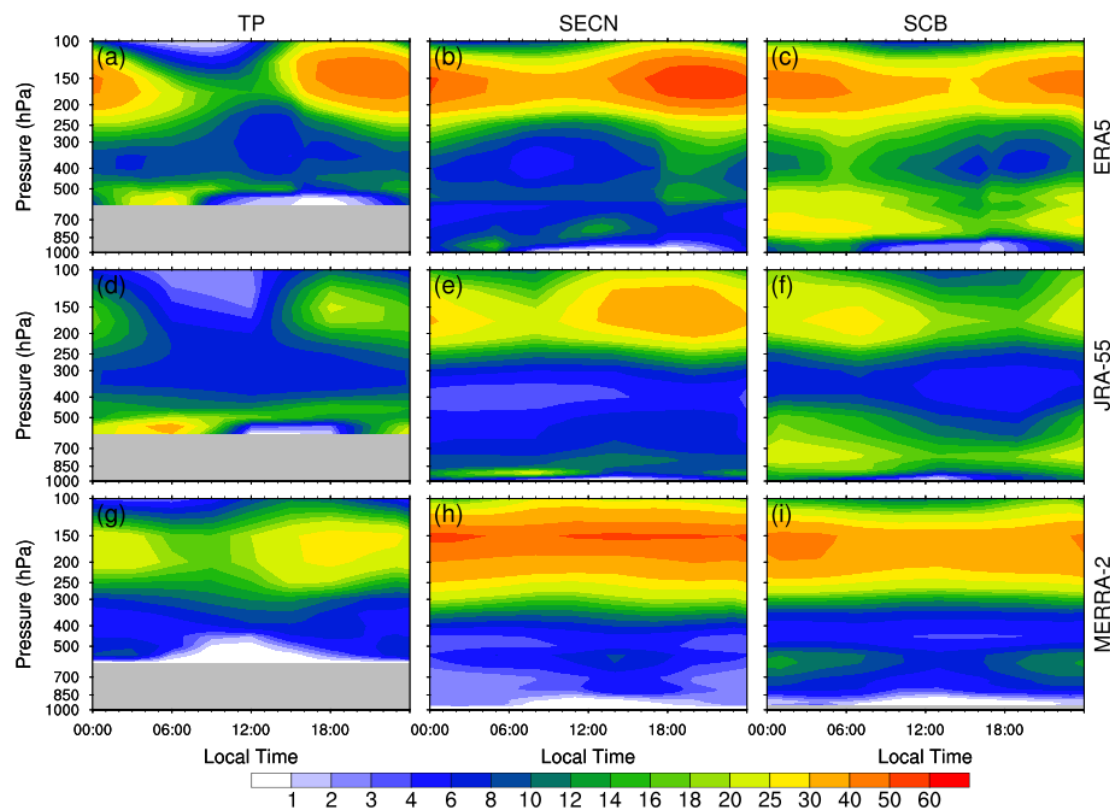
Figure 9. Diurnal variation of cloud fraction over TP (left), SECN (middle) and SCB (right) from ERA5 (top), JRA-55 (middle) and MERRA-2 (bottom). Units: %.
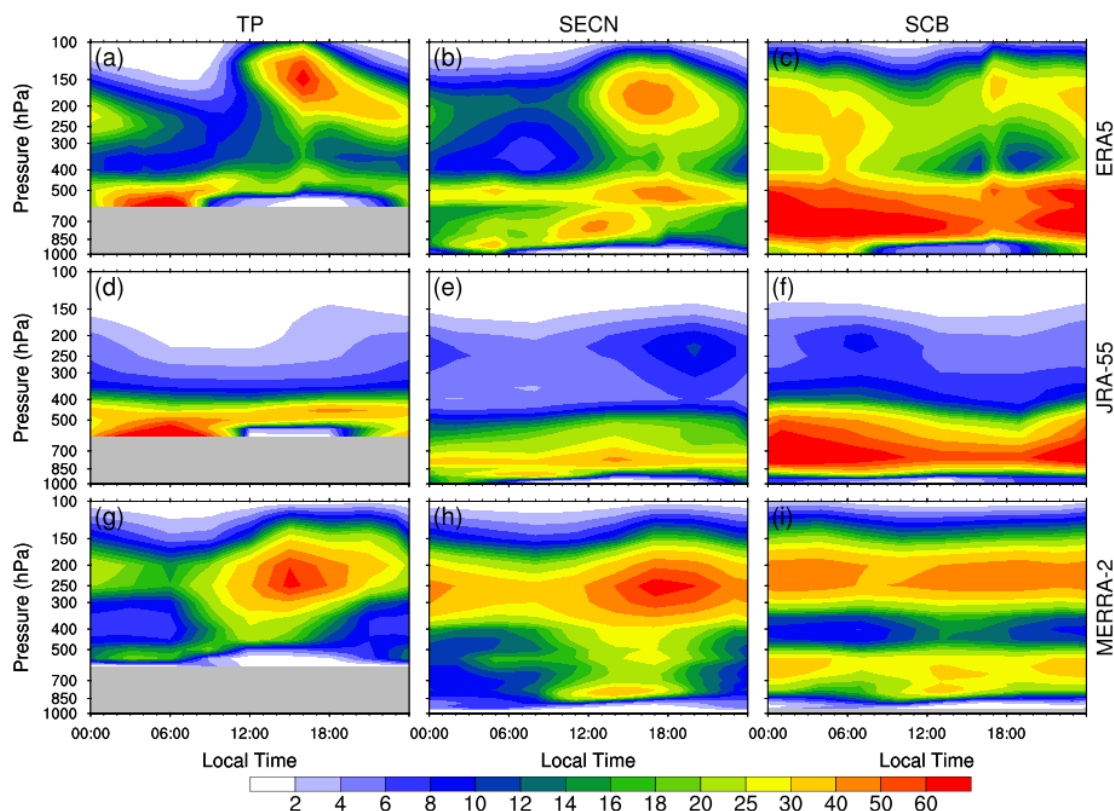
Figure 10. Same as Figure 9, but for cloud hydrometeor content. Units: mg kg⁻¹.

5 Impact of Large-Scale Forcing on DCP

295   The preceding sections have focused on how DCP relates to model physical processes. Large-scale forcing also plays a key role in modulating precipitation characteristics through direct or indirect interactions with these processes. This section therefore analyses several key large-scale forcing variables that influence DCP.

5.1 Vertical Velocity

We first present the diurnal evolution of vertical velocity in Figure 11. Over TP, the evolution is broadly similar among the
300   three reanalyses, with the weakest upward motion around sunrise and the strongest near sunset. The vertical structure in MERRA-2 is more bottom-heavy, with the ascent peaking near 450 hPa, lower than 350 hPa in ERA5 and JRA-55. Over SECN, these inter-model differences become more pronounced. Although all three reanalyses develop with a tilting structure and peak around 15:00 LST, the tilting degree varies markedly. ERA5 exhibits a relatively upright structure, in line with its prematurely developed convection. In comparison, JRA-55 and MERRA-2 exhibit a pronounced tilt, though the ascent in
305   MERRA-2 is noticeably shallower. These tilting structures are consistent with those seen in diabatic heating, demonstrating

that vertical velocity and diabatic heating are well coupled. Over SCB, the strongest ascent in all three reanalyses occurs uniformly around midnight near 700 hPa, coinciding with the nocturnal precipitation maximum and reflecting the region's elevated-convection regime.
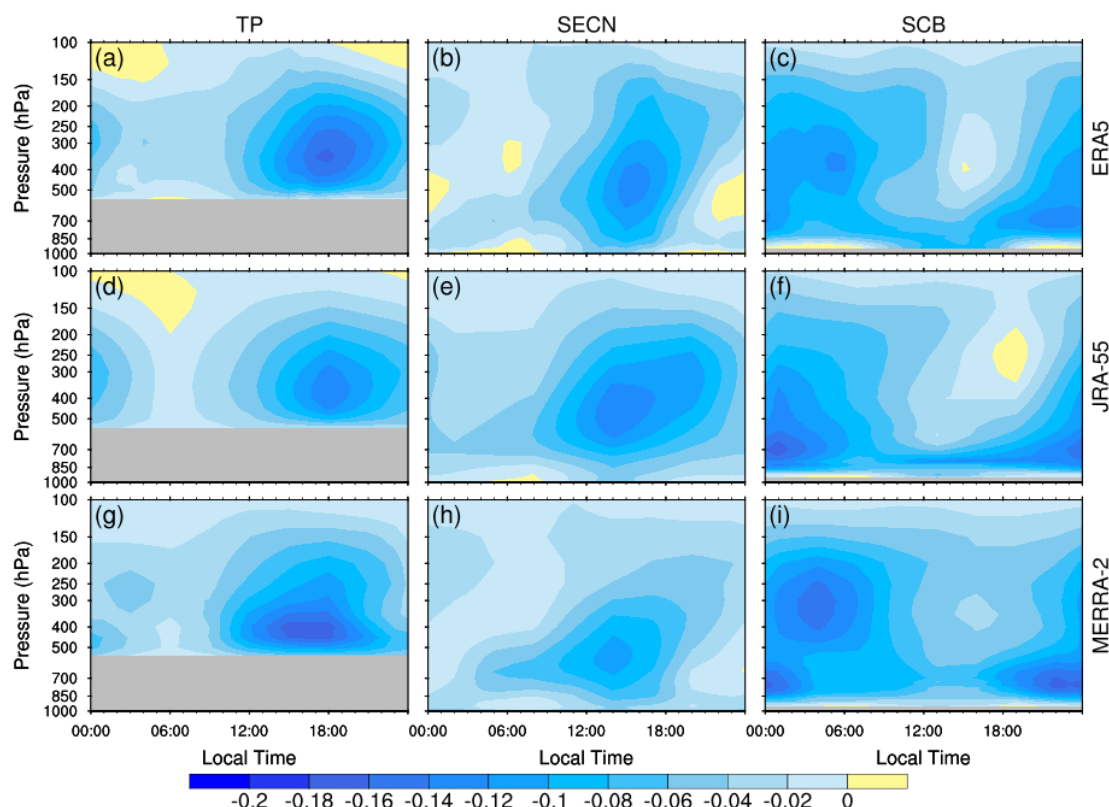
Figure 11. Diurnal variation of vertical velocity over TP (left), SECN (middle) and SCB (right) from ERA5 (top), JRA-55 (middle) and MERRA-2 (bottom). Units: Pa s^{-1}.

Differences in vertical velocity then modulate the vertical advection of dry static energy and moisture (not shown). To quantify how these differences relate to triggering assumptions in convection parameterization, Figure 12 presents the evolution of dynamic convective available potential energy (dCAPE), a measure of the large-scale CAPE generation rate (Wang and Zhang, 2013; Xie and Zhang, 2000). For reference, the corresponding CAPE, calculated following a reversible moist adiabat, and convective precipitation are also plotted. Over TP, dCAPE peaks at a similar time (~18:00 LST) in all three reanalyses despite amplitude differences. Larger dCAPE in ERA5 and MERRA-2 corresponds to their stronger ascent (Figure 11). The dCAPE peak aligns more closely with that of the observed precipitation and lags the CAPE peak, which typically occurs soon after noon. While convective precipitation in ERA5 and MERRA-2 follows CAPE more closely, in JRA-55 it tracks dCAPE better. Over SECN, the lag of dCAPE behind CAPE is less pronounced than over TP, and the influence of triggering choice on precipitation timing is not as obvious as over TP. For SCB, where rainfall is dominated by mid-level elevated convection,

convective precipitation in ERA5 and MERRA-2 aligns closely with CAPE, whereas in JRA-55 it remains better synchronized with dCAPE and matches observations more closely. This contrast underscores how critically the choice of trigger metric

325 influences simulated convective timing, especially over TP and SCB.
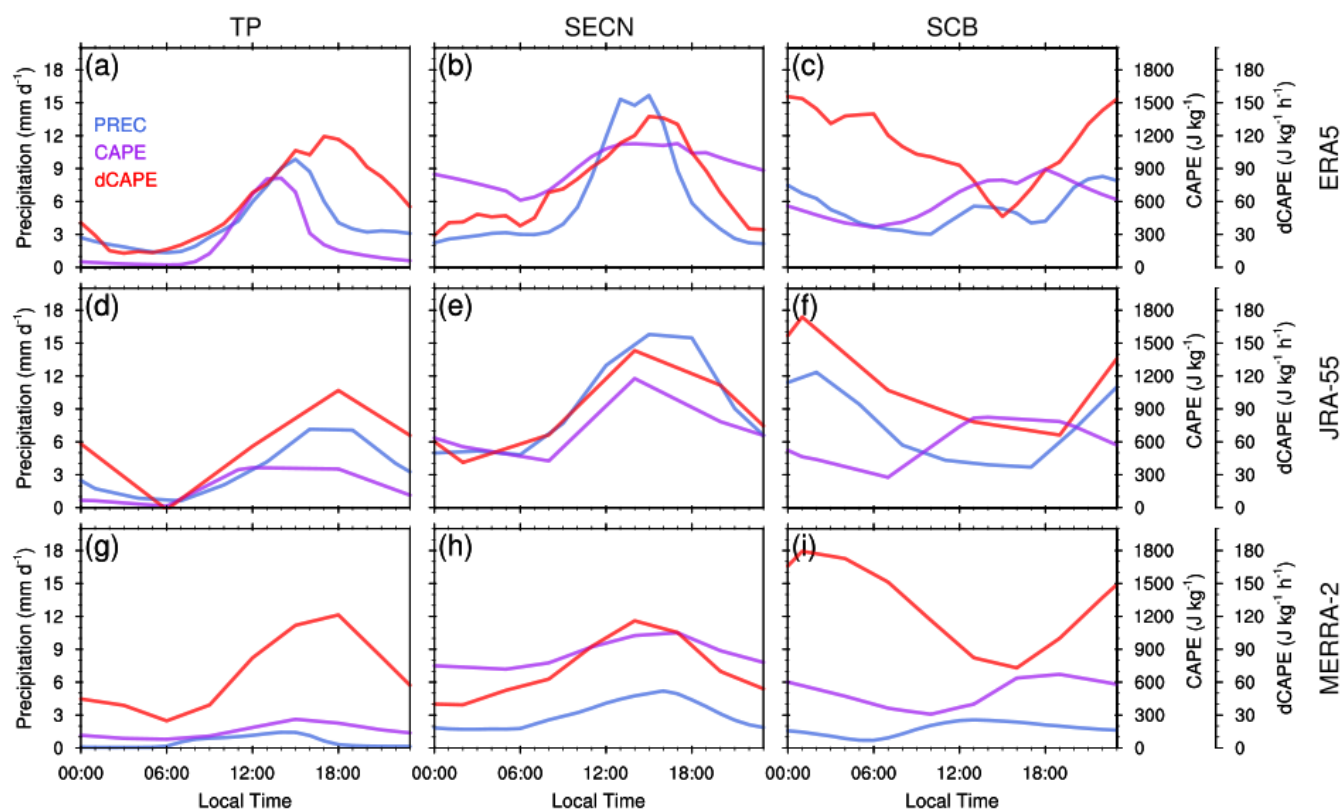
Figure 12. Diurnal variations of convective precipitation, CAPE and dCAPE over TP (left), SECN (middle) and SCB (right) from ERA5 (top), JRA-55 (middle) and MERRA-2 (bottom).

330

5.2 Surface Sensible and Latent Heat Fluxes

The second large-scale forcing examined is surface sensible and latent heat fluxes (Figure 13). In general, surface fluxes in all three datasets peak around noon, although their magnitudes differ substantially. Over TP, ERA5 and JRA-55 show comparable sensible and latent heat fluxes, whereas MERRA-2 produces the strongest sensible heat flux but the weakest latent heat flux,

335 implying a higher Bowen ratio. Over SECN and SCB, the reanalyses exhibit similar sensible heat fluxes, but latent heat flux varies noticeably: strongest in MERRA-2, intermediate in ERA5, and weakest in JRA-55. Since the peak timing of surface fluxes does not coincide with that of precipitation, surface fluxes are unlikely to directly control precipitation timing. Instead, they are more likely to influence convection indirectly by gradually moistening the free troposphere though boundary layer

turbulence and shallow convection. Moreover, the magnitude of surface fluxes does not show a clear relationship with

340 convective precipitation. For instance, smaller latent heat flux in JRA-55 is associated with larger convective precipitation over SECN and SCB, while larger latent heat flux in MERRA-2 corresponds to smaller convective rainfall there. These findings reveal that for deep convection, large-scale forcing within the boundary layer plays a minor role relative to the forcing above the boundary layer.
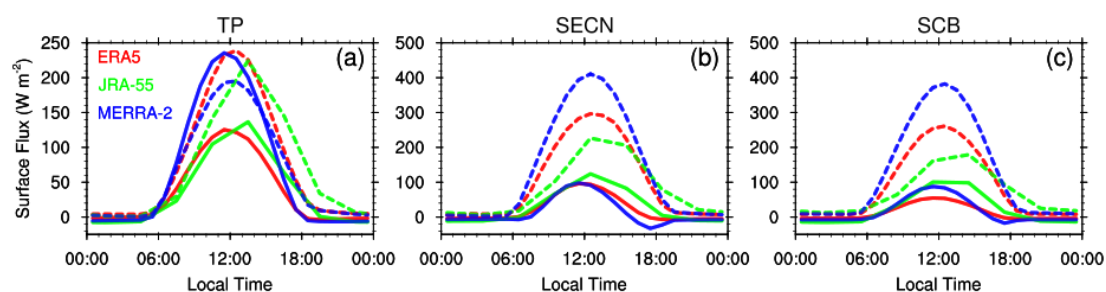
345 **Figure 13. Diurnal variations of sensible (solid) and latent (dashed) heat flux over TP (a), SECN (b) and SCB (c) from ERA5, JRA-55 and MERRA-2.**

6 Conclusions

This study evaluates the performance of three widely used reanalysis datasets—ERA5, JRA-55, and MERRA-2—in simulating the summertime diurnal cycle of precipitation over China. The main conclusions are summarized as follows:

350

Compared with satellite observations (IMERG and CMORPH), JRA-55 reproduces the spatial patterns of DCP phase and amplitude most realistically across China. ERA5 exhibits a systematic phase advance of 2–4 hours, especially in regions dominated by afternoon convection, such as the Tibetan Plateau and southeastern China. MERRA-2 shows pronounced spatial heterogeneity that mixes both leading and lagging phases within areas that appear phase-uniform in observations. Focusing on

355 three representative regions—TP, SECN, and SCB, which represent typical afternoon and nocturnal rainfall regimes, all three reanalyses capture the nocturnal precipitation over SCB, but diverge markedly in simulating afternoon convective rainfall over TP and SECN. Whereas JRA-55 and MERRA-2 reproduce the observed DCP over the TP but show only a slight phase advance (1–2 hours) over SECN, ERA5 exhibits a phase lead of about 3 hours in both regions. Analysis of precipitation partitioning indicates that the early peak in ERA5 is due to its convective component. Like ERA5, MERRA-2 also produces weaker and

360 earlier-peaking convective rainfall, yet much weaker in magnitude, implying that its correct diurnal cycle is achieved largely a result of suppressed convective rainfall.

We further examine diabatic heating and cloud structures to identify the physical processes that shape the simulated DCP. Over TP and SECN, JRA-55 exhibits a gradual development of deep convection, accompanied by a tilted heating structure

365 and subgrid-scale transport of moist static energy that persists into the evening. By contrast, ERA5 develops deep convection

too rapidly, producing premature peaks in diabatic heating and convective eddy transport and thus an earlier rainfall peak. MERRA-2 initiates excessively strong low-level heating and moistening through boundary layer turbulence and shallow convection, which suppresses deep convection and thereby advances the convective rainfall peak. Over SCB, all three reanalyses capture the characteristic elevated-convection by generating nocturnal mid-level heating. Regarding cloud vertical

370   structure, both ERA5 and JRA-55 show a coordinated, upward-tilting growth of cloud fraction and cloud hydrometeor content over TP and SECN, reflecting a realistic transition from shallow to deep convection that aligns with their eddy transport evolution. In MERRA-2, however, only cloud water exhibits a developing tilted structure, while cloud fraction does not. These results indicate that while all three reanalyses reproduce basic heating and cloud features, their internal coherence differs considerably, thus shaping the fidelity of the simulated diurnal cycle.

375

Variations in large-scale forcing are also recognized as a contributor to the simulated discrepancies in DCP. Contrasting vertical velocities modulate the vertical advection of dry static energy and moisture, leading to differences in the large-scale production of CAPE (i.e., dCAPE). The peak timing of dCAPE lags that of CAPE and aligns more closely with the observed precipitation. While convective precipitation in ERA5 and MERRA-2 tracks CAPE more closely, in JRA-55 it aligns better

380   with dCAPE, thereby yielding a more realistic DCP. This contrast highlights the critical influence of triggering choice on cumulus convection. Surface fluxes do not translate into discernible impacts on convective precipitation, suggesting that boundary-layer forcing is subordinate to above-boundary-layer forcing in driving deep convection.

The findings of this study underscore the persistent difficulties in accurately representing DCP over China in current reanalyses.

385   The results not only identify key sources of DCP simulation errors, but also outline practical pathways for improving physical parameterizations in numerical models. Priorities for refinement include trigger mechanisms in convection parameterizations, the transition from shallow to deep convection, and the integrated coupling of boundary layer, convective, and cloud processes.

390   **Appendix A: Fourier Analysis Procedure**

The mean diurnal cycle of precipitation during June-July-August (JJA) is first calculated to obtain a 24-hour time series with a sample size of N=24 /Δt, where Δt is the temporal resolution of the data. Fourier analysis is then applied to decompose the series and extract the diurnal phase and amplitude. The decomposition is expressed as:

$$P = P_0 + P_1(t) + P_2(t) + \cdots + P_{N/2}(t),$$ (A1)

395   $$P_i(t) = A_i \cos\left(\frac{2\pi}{N}(it - \varphi_i)\right),$$ (A2)

where P_0 is the daily mean precipitation, t is the time, $P_i(t)$ is the i-th harmonic component, and A_i and φ_i are its corresponding amplitude and phase. In this study, the first harmonic component (i=1) is adopted to represent the diurnal cycle for analysis.

Data availability

400 CMORPH can be obtained from https://www.ncei.noaa.gov/products (NOAA National Centers for Environmental Information, 2025). The ERA5 datasets are available from https://cds.climate.copernicus.eu (Copernicus Climate Data Store, 2025). The IMERGE and MERRA-2 products are obtained from https://daac.gsfc.nasa.gov (NASA Goddard Earth Sciences Data and Information Services Center, 2025). JRA-55 products were acquired from https://gdex.ucar.edu (Geoscience Data Exchange, 2025).

Author contribution

405

YL: data curation, formal analysis, investigation, validation, visualization, writing (original draft), writing (review and editing). XW: conceptualization, funding acquisition, methodology, supervision, validation, writing (review and editing). YL: resources, supervision, validation, writing (review and editing). ST: supervision, validation, writing (review and editing). HM: validation, writing (review and editing).

Competing interests

410

The authors declare that they have no conflict of interest.

Disclaimer

Publisher's note: Copernicus Publications remains neutral with regard to jurisdictional claims in published maps and institutional affiliations.

Acknowledgements

415

The authors would like to thank the GPM, CMORPH, ERA5, JRA-55 and MERRA-2 science teams for providing excellent and accessible data products that made this study possible.

Financial support

This research is jointly supported by the National Key Research and Development Program of China (Grants
2022YFF0802003), the National Natural Science Foundation of China (Grants 42575163, 42175165), and the National Key
Scientific and Technological Infrastructure project "Earth System Science Numerical Simulator Facility" (EarthLab).

References

Bao, X. and Zhang, F.: Impacts of the mountain–plains solenoid and cold pool dynamics on the diurnal variation of warm-season precipitation over northern China, Atmospheric Chem. Phys., 13, 6965–6982, https://doi.org/10.5194/acp-13-6965-2013, 2013.

Bechtold, P., Chaboureau, J. -P., Beljaars, A., Betts, A. K., Köhler, M., Miller, M., and Redelsperger, J. -L.: The simulation of the diurnal cycle of convective precipitation over land in a global model, Q. J. R. Meteorol. Soc., 130, 3119–3137, https://doi.org/10.1256/qj.03.103, 2004.

Bechtold, P., Köhler, M., Jung, T., Doblas-Reyes, F., Leutbecher, M., Rodwell, M. J., Vitart, F., and Balsamo, G.: Advances in simulating atmospheric variability with the ECMWF model: From synoptic to decadal time-scales, Q. J. R. Meteorol. Soc., 134, 1337–1351, https://doi.org/10.1002/qj.289, 2008.

Bechtold, P., Semane, N., Lopez, P., Chaboureau, J.-P., Beljaars, A., and Bormann, N.: Representing Equilibrium and Nonequilibrium Convection in Large-Scale Models, J. Atmospheric Sci., 71, 734–753, https://doi.org/10.1175/JAS-D-13-0163.1, 2014.

Carbone, R. E. and Tuttle, J. D.: Rainfall occurrence in the U.S. warm season: The diurnal cycle, J. Clim., 21, 4132–4146, https://doi.org/10.1175/2008JCLI2275.1, 2008.

Chen, G., Sha, W., Iwasaki, T., and Wen, Z.: Diurnal cycle of a heavy rainfall corridor over east Asia, Mon. Weather Rev., 145, 3365–3389, https://doi.org/10.1175/MWR-D-16-0423.1, 2017.

Covey, C., Gleckler, P. J., Doutriaux, C., Williams, D. N., Dai, A., Fasullo, J., Trenberth, K., and Berg, A.: Metrics for the diurnal cycle of precipitation: Toward routine benchmarks for climate models, J. Clim., 29, 4461–4471, https://doi.org/10.1175/JCLI-D-15-0664.1, 2016.

Dai, A.: Global precipitation and thunderstorm frequencies. Part II: Diurnal variations, J. Clim., 14, 1112–1128, https://doi.org/10.1175/1520-0442(2001)014%253C1112:GPATFP%253E2.0.CO;2, 2001.

Dai, A. and Trenberth, K. E.: The diurnal cycle and its depiction in the community climate system model, J. Clim., 17, 930–951, https://doi.org/10.1175/1520-0442(2004)017%253C0930:TDCAID%253E2.0.CO;2, 2004.

Gelaro, R., McCarty, W., Suárez, M. J., Todling, R., Molod, A., Takacs, L., Randles, C. A., Darmenov, A., Bosilovich, M. G., Reichle, R., Wargan, K., Coy, L., Cullather, R., Draper, C., Akella, S., Buchard, V., Conaty, A., Da Silva, A. M., Gu, W., Kim, G.-K., Koster, R., Lucchesi, R., Merkova, D., Nielsen, J. E., Partyka, G., Pawson, S., Putman, W., Rienecker, M., Schubert, S. D., Sienkiewicz, M., and Zhao, B.: The modern-era retrospective analysis for research and applications, version 2 (MERRA-2), J. Clim., 30, 5419–5454, https://doi.org/10.1175/JCLI-D-16-0758.1, 2017.

Hersbach, H., Bell, B., Berrisford, P., Hirahara, S., Horányi, A., Muñoz-Sabater, J., Nicolas, J., Peubey, C., Radu, R., Schepers, D., Simmons, A., Soci, C., Abdalla, S., Abellan, X., Balsamo, G., Bechtold, P., Biavati, G., Bidlot, J., Bonavita, M., De Chiara, G., Dahlgren, P., Dee, D., Diamantakis, M., Dragani, R., Flemming, J., Forbes, R., Fuentes, M., Geer, A., Haimberger, L., Healy, S., Hogan, R. J., Hólm, E., Janisková, M., Keeley, S., Laloyaux, P., Lopez, P., Lupu, C., Radnoti, G., De Rosnay, P., 455 Rozum, I., Vamborg, F., Villaume, S., and Thépaut, J.: The ERA5 global reanalysis, Q. J. R. Meteorol. Soc., 146, 1999–2049, https://doi.org/10.1002/qj.3803, 2020.

Huffman, G. J., Stocker, E. F., Bolvin, D. T., Nelkin, E. J., and Tan, J.: GPM IMERG Final Precipitation L3 Half Hourly 0.1 degree x 0.1 degree V07, https://doi.org/10.5067/GPM/IMERG/3B-HH/07, 2023.

Khairoutdinov, M. and Randall, D.: High-Resolution Simulation of Shallow-to-Deep Convection Transition over Land, J. 460 Atmospheric Sci., 63, 3421–3436, https://doi.org/10.1175/JAS3810.1, 2006.

Kobayashi, S., Ota, Y., Harada, Y., Ebita, A., Moriya, M., Onoda, H., Onogi, K., Kamahori, H., Kobayashi, C., Endo, H., Miyaoka, K., and Takahashi, K.: The JRA-55 reanalysis: General specifications and basic characteristics, J. Meteorol. Soc. Jpn., 93, 5–48, https://doi.org/10.2151/jmsj.2015-001, 2015.

Koo, M. and Hong, S.: Diurnal variations of simulated precipitation over east Asia in two regional climate models, J. Geophys. 465 Res. Atmospheres, 115, 2009JD012574, https://doi.org/10.1029/2009JD012574, 2010.

Lee, M.-I., Schubert, S. D., Suarez, M. J., Held, I. M., Lau, N.-C., Ploshay, J. J., Kumar, A., Kim, H.-K., and Schemm, J.-K. E.: An analysis of the warm-season diurnal cycle over the continental united states and northern mexico in general circulation models, J. Hydrometeorol., 8, 344–366, https://doi.org/10.1175/JHM581.1, 2007.

Lee, M.-I., Schubert, S. D., Suarez, M. J., Schemm, J.-K. E., Pan, H.-L., Han, J., and Yoo, S.-H.: Role of convection triggers 470 in the simulation of the diurnal cycle of precipitation over the united states great plains in a general circulation model, J. Geophys. Res. Atmospheres, 113, D02111, https://doi.org/10.1029/2007JD008984, 2008.

Li, J., Yu, R., and Zhou, T.: Seasonal variation of the diurnal cycle of rainfall in southern contiguous China, J. Clim., 21, https://doi.org/10.1175/2008JCLI2188.1, 2008.

Lin, L., Gettelman, A., Xu, Y., Wu, C., Wang, Z., Rosenbloom, N., Bates, S. C., and Dong, W.: CAM6 simulation of mean 475 and extreme precipitation over Asia: Sensitivity to upgraded physical parameterizations and higher horizontal resolution, Geosci. Model Dev., 12, 3773–3793, https://doi.org/10.5194/gmd-12-3773-2019, 2019.

Ma, H.-Y., Zhou, C., Zhang, Y., Klein, S. A., Zelinka, M. D., Zheng, X., Xie, S., Chen, W.-T., and Wu, C.-M.: A multi-year short-range hindcast experiment with CESM1 for evaluating climate model moist processes from diurnal to interannual timescales, Geosci. Model Dev., 14, 73–90, https://doi.org/10.5194/gmd-14-73-2021, 2021.

480 Miao, H., Wang, X., Liu, Y., and Wu, G.: An evaluation of cloud vertical structure in three reanalyses against CloudSat/cloud-aerosol lidar and infrared pathfinder satellite observations, Atmospheric Sci. Lett., 20, e906, https://doi.org/10.1002/asl.906, 2019.

Molod, A., Takacs, L., Suarez, M., and Bacmeister, J.: Development of the GEOS-5 atmospheric general circulation model: Evolution from MERRA to MERRA2, Geosci. Model Dev., 8, 1339–1356, https://doi.org/10.5194/gmd-8-1339-2015, 2015.

485 Pradhan, R. K., Markonis, Y., Marra, F., Nikolopoulos, E. I., Papalexiou, S. M., and Levizzani, V.: Diurnal variability of global precipitation: Insights from hourly satellite and reanalysis datasets, Hydrol. Earth Syst. Sci., 29, 4929–4949, https://doi.org/10.5194/hess-29-4929-2025, 2025.

Rio, C., Hourdin, F., Grandpeix, J. -Y., and Lafore, J. -P.: Shifting the diurnal cycle of parameterized deep convection over land, Geophys. Res. Lett., 36, 2008GL036779, https://doi.org/10.1029/2008GL036779, 2009.

490   Shen, Y., Xiong, A., Wang, Y., and Xie, P.: Performance of high-resolution satellite precipitation products over China, J. Geophys. Res. Atmospheres, 115, D02114, https://doi.org/10.1029/2009JD012097, 2010.

Song, H., Zhang, Z., Ma, P.-L., Ghan, S. J., and Wang, M.: An evaluation of marine boundary layer cloud property simulations in the community atmosphere model using satellite observations: Conventional subgrid parameterization versus CLUBB, J. Clim., 31, 2299–2320, https://doi.org/10.1175/JCLI-D-17-0277.1, 2018.

495   Song, Y. and Wei, J.: Diurnal cycle of summer precipitation over the north China plain and associated land–atmosphere interactions: Evaluation of ERA5 and MERRA-2, Int. J. Climatol., 41, 6031–6046, https://doi.org/10.1002/joc.7166, 2021.

Tang, S., Gleckler, P., Xie, S., Lee, J., Ahn, M.-S., Covey, C., and Zhang, C.: Evaluating the diurnal and semidiurnal cycle of precipitation in CMIP6 models using satellite- and ground-based observations, J. Clim., 34, 3189–3210, https://doi.org/10.1175/jcli-d-20-0639.1, 2021.

500   Tang, S., Xie, S., Guo, Z., Hong, S., Khouider, B., Klocke, D., Köhler, M., Koo, M., Krishna, P. M., Larson, V. E., Park, S., Vaillancourt, P. A., Wang, Y., Yang, J., Daleu, C. L., Homeyer, C. R., Jones, T. R., Malap, N., Neggers, R., Prabhakaran, T., Ramirez, E., Schumacher, C., Tao, C., Bechtold, P., Ma, H., Neelin, J. D., and Zeng, X.: Long-term single-column model intercomparison of diurnal cycle of precipitation over midlatitude and tropical land, Q. J. R. Meteorol. Soc., 148, 641–669, https://doi.org/10.1002/qj.4222, 2022.

505   Tao, C., Xie, S., Ma, H., Bechtold, P., Cui, Z., Vaillancourt, P. A., Van Weverberg, K., Wang, Y., Wong, M., Yang, J., Zhang, G. J., Choi, I., Tang, S., Wei, J., Wu, W., Zhang, M., Neelin, J. D., and Zeng, X.: Diurnal cycle of precipitation over the tropics and central United States: intercomparison of general circulation models, Q. J. R. Meteorol. Soc., 150, 911–936, https://doi.org/10.1002/qj.4629, 2024.

Trenberth, K. E., Dai, A., Rasmussen, R. M., and Parsons, D. B.: The changing character of precipitation, Bull. Am. Meteorol.
510   Soc., 84, 1205–1218, https://doi.org/10.1175/BAMS-84-9-1205, 2003.

Wang, X. and Zhang, M.: An analysis of parameterization interactions and sensitivity of single-column model simulations to convection schemes in CAM4 and CAM5, J. Geophys. Res. Atmospheres, 118, 8869–8880, https://doi.org/10.1002/jgrd.50690, 2013.

Wang, Y., Xie, S., Tang, S., and Lin, W.: Evaluation of an Improved Convective Triggering Function: Observational Evidence
515   and SCM Tests, J. Geophys. Res. Atmospheres, 125, e2019JD031651, https://doi.org/10.1029/2019JD031651, 2020.

Wang, Y.-C., Pan, H.-L., and Hsu, H.-H.: Impacts of the triggering function of cumulus parameterization on warm-season diurnal rainfall cycles at the atmospheric radiation measurement southern great plains site, J. Geophys. Res. Atmospheres, 120, 10681–10702, https://doi.org/10.1002/2015JD023337, 2015.

Wright, J. S., Sun, X., Konopka, P., Krüger, K., Legras, B., Molod, A. M., Tegtmeier, S., Zhang, G. J., and Zhao, X.:
520   Differences in tropical high clouds among reanalyses: Origins and radiative impacts, Atmospheric Chem. Phys., 20, 8989–9030, https://doi.org/10.5194/acp-20-8989-2020, 2020.

Xie, P., Joyce, R., Wu, S., Yoo, S.-H., Yarosh, Y., Sun, F., Lin, R., and NOAA CDR Program: NOAA climate data record (CDR) of CPC morphing technique (CMORPH) high resolution global precipitation estimates, version 1, https://doi.org/10.25921/w9va-q159, 2019a.

525   Xie, S. and Zhang, M.: Impact of the convection triggering function on single-column model simulations, J. Geophys. Res. Atmospheres, 105, 14983–14996, https://doi.org/10.1029/2000JD900170, 2000.

Xie, S., Wang, Y., Lin, W., Ma, H., Tang, Q., Tang, S., Zheng, X., Golaz, J., Zhang, G. J., and Zhang, M.: Improved diurnal cycle of precipitation in E3SM with a revised convective triggering function, J. Adv. Model. Earth Syst., 11, 2290–2310, https://doi.org/10.1029/2019MS001702, 2019b.

530   Yang, B., Zhou, Y., Zhang, Y., Huang, A., Qian, Y., and Zhang, L.: Simulated precipitation diurnal cycles over east Asia using different CAPE-based convective closure schemes in WRF model, Clim. Dyn., 50, 1639–1658, https://doi.org/10.1007/s00382-017-3712-z, 2018.

Yang, M., Liu, J., Wang, Y., Chen, J. M., Cui, Z., Zhang, Z., Chen, Z., and Cheng, X.: Prominent impact of diurnal rainfall variations on evapotranspiration and gross primary productivity in forests over low latitudes, Agric. For. Meteorol., 342, 535   109740, https://doi.org/10.1016/j.agrformet.2023.109740, 2023.

Yu, R., Zhou, T., Xiong, A., Zhu, Y., and Li, J.: Diurnal variations of summer precipitation over contiguous China, Geophys. Res. Lett., 34, 2006GL028129, https://doi.org/10.1029/2006GL028129, 2007.

Yuan, W.: Diurnal cycles of precipitation over subtropical China in IPCC AR5 AMIP simulations, Adv. Atmospheric Sci., 30, 1679–1694, https://doi.org/10.1007/s00376-013-2250-9, 2013.

540   Zhang, B., Donner, L. J., Zhao, M., and Tan, Z.: Improved precipitation diurnal cycle in GFDL climate models with non-equilibrium convection, J. Adv. Model. Earth Syst., 16, e2024MS004315, https://doi.org/10.1029/2024MS004315, 2024.

Zhang, C., Wang, D., Pang, Z., and Jiang, X.: Observed large-scale structures and diabatic heating profiles of precipitation over the tibetan plateau and south China, J. Geophys. Res. Atmospheres, 126, e2020JD033949, https://doi.org/10.1029/2020JD033949, 2021.

545   Zhang, G. J.: Convective quasi-equilibrium in midlatitude continental environment and its effect on convective parameterization, J. Geophys. Res. Atmospheres, 107, 4220, https://doi.org/10.1029/2001JD001005, 2002.

Zhang, Y., Zhang, F., and Sun, J.: Comparison of the diurnal variations of warm-season precipitation for East Asia vs. North America downstream of the Tibetan Plateau vs. the Rocky Mountains, Atmospheric Chem. Phys., 14, 10741–10759, https://doi.org/10.5194/acp-14-10741-2014, 2014.

550